

Rate-Splitting–Inspired Bistatic OFDM-ISAC

Bruno F. Costa, *Student Member, IEEE*, Anup Mishra, *Member, IEEE*, Israel Leyva-Mayorga, *Member, IEEE*, Taufik Abrão, *Senior Member, IEEE*, and Petar Popovski, *Fellow, IEEE*

Abstract—Achieving effective uplink bistatic integrated sensing and communication (ISAC) over an orthogonal frequency division multiplexing (OFDM) waveform gives rise to challenging interference structures. These are mostly due to unequal direct- and echo-path contributions and Doppler-induced inter-carrier interference (ICI), rendering orthogonal resource separation and fixed successive interference cancellation (SIC) strategies inadequate. To address this problem, we propose a rate-splitting (RS)-inspired framework where the transmitter splits each communication message into a robust and a supplementary stream, which are jointly superposed over a sensing signal. Furthermore, we present the design of a staged sensing–communication receiver. Based on this framework, we derive tractable per-subcarrier signal-to-interference-plus-noise ratio (SINR) expressions and establish the relation between sensing accuracy and communication reliability based on the Fisher information. Building on these, we formulate a joint power-allocation problem for spectral efficiency (SE) maximization under sensing-performance and power constraints. The resulting non-convex formulation is solved using convex surrogates and fractional programming. Numerical results demonstrate that, compared to non-orthogonal multiple access (NOMA)-inspired baselines, the proposed framework provides more effective inter-functionality interference (IFI) management and improved robustness to Doppler-induced ICI.

Index Terms—OFDM-ISAC, multiple-access, rate-splitting (RS), inter-functionality interference management

I. INTRODUCTION

Integrated sensing and communication (ISAC) has been touted as a key enabling technology for sixth-generation (6G) wireless networks, driven by the growing convergence of spectrum usage, hardware platforms, and signal processing pipelines for communication and sensing [1]–[4]. By allowing the same wireless infrastructure to provide both connectivity and environmental awareness, ISAC promises gains in spectral and energy efficiency while enabling applications such as intelligent transportation, remote monitoring, and autonomous systems [1], [5]. These gains, however, come at the cost of more intricate interaction between communication and sensing, since sharing spectral resources, waveform dimensions, and receiver processing makes mutual interference unavoidable [6]. Consequently, interference management emerges as a defining design challenge in ISAC, rather than a secondary implementation issue [2], [4], [6].

From an interference-centric viewpoint, ISAC departs from conventional communication-only and sensing-only systems because several interference mechanisms coexist and interact [6]–[8]. Recent literature broadly classifies these into clutter interference, self-interference, inter-target interference, inter-user

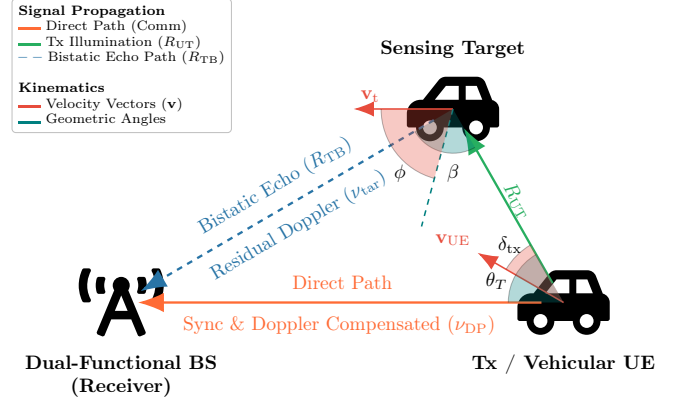


Figure 1: Uplink bistatic ISAC geometry. The relative velocities v_{UE} and v_t , along with angles δ_{tx} , θ_T , and β , define the doubly-selective channel characteristics.

interference, and inter-functionality interference (IFI) between communication and sensing [2], [6], [9]. Of these interference types, IFI is particularly critical in highly integrated and non-orthogonal ISAC architectures, where the two functionalities operate over shared resources and processing chains [8], [10]. In uplink bistatic ISAC scenarios, as illustrated in Fig. 1, IFI can become especially pronounced when the direct and echo paths contribute unequally to communication and sensing, with its severity jointly governed by their relative strengths and the receiver processing strategy [11]–[13]. This imbalance-driven IFI is further compounded in mobile orthogonal frequency division multiplexing (OFDM) settings, where Doppler-induced loss of subcarrier orthogonality introduces an additional layer of interference in the form of echo-path (EP) inter-carrier interference (ICI) [12], [14], [15].

These considerations naturally motivate the use of multiple-access design principles for interference management in ISAC. Taking inspiration from multiple access schemes managing *inter-user interference* in communication-only systems, existing works have adapted strategies such as resource partitioning, and superposition and successive decoding to manage IFI between coexisting sensing and communication signals [6]–[8]. In this context, orthogonal multiple access (OMA)-inspired ISAC suppresses interference through resource separation, but at the cost of reduced spectral efficiency (SE). Non-orthogonal multiple access (NOMA)-inspired ISAC improves resource utilization through superposition and successive interference cancellation (SIC), yet inherits a rigid decoding structure that may leave one functionality strongly interference-limited by the other [2], [7]. To overcome these limitations, rate-splitting (RS)-inspired ISAC was introduced as a more flexible framework, generalizing the non-orthogonal design principle of NOMA-inspired designs by allowing *one functionality to*

B. F. Costa and T. Abrão are with the Department of Electrical Engineering, State University of Londrina (UEL), Londrina, PR, 86057-970, Brazil (e-mail: bruno.felipe.costa@uel.br; taufik@uel.br)

A. Mishra, I. Leyva-Mayorga, and P. Popovski are with the Department of Electronic Systems, Aalborg University, Denmark (e-mail: anmi@es.aau.dk; ilm@es.aau.dk; petarp@es.aau.dk).

be recovered through partial decoding of the other while treating the remaining interference as noise [3]. Such flexibility is particularly attractive for managing IFI in ISAC settings where the sensing-communication coupling evolves across propagation conditions and receiver stages, while practical impairments further complicate the resulting interference structure, exposing the limitations of both OMA- and NOMA-inspired strategies [3], [16]–[18].

Motivated by the above considerations, we propose and investigate an RS-inspired uplink bistatic OFDM-ISAC framework in which a vehicular user equipment (UE) transmits a superposed communication-sensing waveform to a network base station (BS) while simultaneously illuminating a traffic target. The BS acts as a dual-functional bistatic receiver, where the direct and target-echo paths jointly contribute to the received communication signal, while the echo path additionally conveys the target delay-Doppler information required for sensing. In mobile OFDM settings, after synchronization to the dominant direct path, subcarrier orthogonality can be largely restored for the main communication link, whereas the residual bistatic Doppler of the echo remains uncompensated, causing Doppler-induced ICI across subcarriers [11], [17], [19]. Accordingly, the proposed framework addresses these coupled impairments by using RS-inspired layered decoding, sensing, and interference cancellation to manage IFI, while explicitly incorporating echo-path ICI into the sensing, reconstruction, and suppression stages. Numerical results demonstrate that the proposed RS-inspired ISAC framework outperforms NOMA-inspired baselines in managing IFI, while also exhibiting greater robustness to ICI.

A. Related Works

Multiple-access-focused ISAC research has developed along several complementary directions. On the one hand, multiple-access-assisted ISAC schemes use multiple-access techniques primarily for inter-user interference management, while handling IFI implicitly or through sensing-communication co-design. Reference [20] proposes a multi-antenna rate-splitting multiple access (RSMA)-based dual-functional radar-communication architecture that improves the weighted-sum-rate and radar beam pattern trade-off over space-division multiple access (SDMA)-assisted and orthogonal baselines. Tutorial [21] further reviews related extensions of this line, including RS-based joint radar-communication transmission under partial channel state information at the transmitter (CSIT) and RSMA-assisted dual-functional radar-communication satellite systems. Subsequently, [22] studies an uplink RSMA-enabled ISAC system where RS is applied across communication users to mitigate inter-user interference and enhance sensing performance over OMA and NOMA baselines. On the other hand, multiple-access-inspired ISAC works have addressed IFI by explicitly borrowing multiple-access principles from communication-only systems. Reference [8] develops inner bounds for radar-communication coexistence in shared spectrum under isolated-subband and SIC-based operating regimes. Reference [23] studies a downlink ISAC design in which part of the dedicated sensing signal is treated as virtual communication signals and mitigated via SIC, together with joint communication-sensing signal optimization. References [7], [10] further develop

downlink and uplink NOMA-based ISAC designs, including pure-NOMA- and semi-NOMA-based uplink architectures for mixed sensing-communication reception at the BS. More recently, [3] develops an RS-inspired coexistence framework in which the communication message is split into multiple streams, enabling more flexible decoding-order control between communication and sensing than OMA- and NOMA-inspired baselines. Broader overviews of related multiple-access-focused ISAC designs in various settings are provided in [2], [6], [21].

A separate but closely related line of work has focused on uplink bistatic and OFDM-based ISAC, together with receiver architectures relevant to this setting. In [19], an uplink joint communication and sensing system with physically separated transceivers is analyzed, explicitly accounting for the impact of line-of-sight (LoS)-path noise and communication decoding errors on delay-Doppler estimation. Bi-static sensing with 5th generation (5G) new radio (NR) physical uplink shared channel transmissions is investigated in [24], which highlights practical bottlenecks such as limited UE transmit power and the path-loss imbalance between the direct and echo links. A bistatic OFDM-based ISAC concept with over-the-air synchronization is then developed in [11], where the impact of residual synchronization mismatches and communication decoding failures on both radar and communication performance is analyzed. Complementing these setting-focused works, [13] develops a flexible uplink ISAC receiver framework that bridges projection-type and SIC-type processing through a tunable tradeoff factor, highlighting the benefit of stage-adaptive receiver design. On the RS side, [25] studies a framework for low earth orbit (LEO) satellite systems, where the common stream is jointly exploited for radar beamforming, inter-user interference management, and IFI management under Cramér-Rao lower bound (CRLB) constraints. Finally, regarding robustness to Doppler-induced ICI, [17] shows in a communication-only OFDM setting that RSMA benefits from the ability to partially decode interference while treating the remainder as noise [16].

B. Motivation and Contributions

Despite recent progress on multiple-access-focused ISAC, uplink bistatic sensing, and robust OFDM-RSMA transmission, a unified treatment of these aspects remains unavailable. In particular, the existing literature does not provide an RS-inspired uplink bistatic OFDM-ISAC framework in which IFI and echo-path ICI are jointly addressed through staged receiver processing and power allocation. This gap is especially relevant in uplink bistatic OFDM settings, where the direct and reflected paths contribute unequally to communication and sensing, and where residual bistatic Doppler further complicates receiver operation through ICI. Motivated by this gap and building upon the foundational RS-inspired coexistence framework in [3], this paper makes the following contributions.

- We propose an RS-inspired uplink bistatic OFDM-ISAC signal model for doubly selective channels, in which the communication message is split into a robust stream and a supplementary stream, and both are superposed with a deterministic radar sequence. The formulation captures the coexistence of direct-path (DP) and EP com-

ponents, together with the resulting asymmetric sensing–communication coupling.

- We develop a staged receiver architecture tailored to this setting, comprising DP radar cancellation, robust-stream decoding, target parameter estimation, echo reconstruction, and supplementary-stream decoding. Based on this receiver, we derive tractable per-subcarrier signal-to-interference-plus-noise ratio (SINR) expressions that account for DP interference, EP interference, Doppler-induced ICI, and echo-reconstruction mismatch.
- We establish an explicit link between sensing accuracy and communication reliability through a CRLB-based analysis. Specifically, we derive the Fisher-information-based delay–Doppler estimation accuracy and map it to the residual echo-channel reconstruction error, thereby quantifying how sensing uncertainty propagates into the decoding performance of the supplementary communication stream.
- We formulate a power-allocation problem that maximizes communication SE subject to sensing-accuracy and power constraints. To solve the resulting non-convex design, we develop a tractable framework based on linear matrix inequality (LMI)-based surrogates, convex approximations of the reconstruction-mismatch term, and multidimensional fractional programming.
- Through numerical results, we show that the proposed RS-inspired design outperforms NOMA-inspired baselines across static and mobile regimes. In particular, it provides more flexible IFI management in the zero-mobility case and exhibits greater robustness to EP ICI under Doppler.

Taken together, these contributions extend the RS-inspired ISAC framework of [3] from a simplified coexistence setting to an uplink bistatic OFDM architecture with explicit delay–Doppler coupling, staged sensing–communication receiver interaction, and joint treatment of IFI and ICI. To the best of our knowledge, this is the first work to investigate an RS-inspired ISAC framework for the joint treatment of these two impairments.

Notations: Scalars are denoted by lowercase italic (x); vectors by bold lowercase (\mathbf{x}); parameter vectors by bold italic (e.g., $\boldsymbol{\theta}$); and matrices by bold uppercase (\mathbf{X}). The sets \mathbb{R} , \mathbb{C} , and \mathbb{Z} denote real numbers, complex numbers, and integers, respectively, $\mathcal{CN}(\boldsymbol{\mu}, \boldsymbol{\Sigma})$ denotes a circularly symmetric complex Gaussian (CSCG) distribution with mean $\boldsymbol{\mu}$ and covariance $\boldsymbol{\Sigma}$, and $\mathcal{U}[a, b)$ denotes the continuous uniform distribution over the interval $[a, b)$. We use $(\cdot)^*$ for complex conjugate, $(\cdot)^H$ for Hermitian transpose, $\mathbb{E}[\cdot]$ for expectation, $\det(\cdot)$ for determinant, and $\Re\{\cdot\}$, $\Im\{\cdot\}$ for real and imaginary parts.

Organization: The remainder of this paper is organized as follows. Section II introduces the uplink bistatic OFDM-ISAC system model, including the RS-inspired superposition transmission model. Section III presents the staged receiver, derives the per-subcarrier SINR expressions, and develops the associated estimation-accuracy and channel-reconstruction error analyses. Section IV formulates the sensing-constrained power-allocation problem. Section V provides numerical results and benchmarks the proposed framework against NOMA-inspired baselines. Finally, Section VI concludes the paper.

II. SYSTEM MODEL

We consider the uplink bistatic vehicle-to-network (V2N) ISAC architecture illustrated in Fig. 1. A vehicular UE transmits an uplink OFDM waveform to a network BS while simultaneously illuminating a traffic target, e.g., another vehicle. The BS acts as a dual-functional bistatic receiver tasked with decoding the uplink communication streams and estimating the kinematic parameters of the target echo. Both the direct and echo paths contain replicas of the transmitted superposed waveform; however, owing to the two-way propagation loss and target scattering, the echo-path signal is typically much weaker than the direct-path component and additionally carries the target-dependent delay-Doppler information required for sensing [24], [26]. Consequently, the strong DP component acts as a dominant disturbance to sensing, while the EP component also remains a source of residual interference during communication decoding.

A. RS-Inspired Superposition OFDM Transmission

Let $n \in \mathcal{N} = \{-N_{sc}/2, \dots, N_{sc}/2 - 1\}$ denote the subcarrier index and $m \in \{0, \dots, M - 1\}$ the OFDM symbol index. Following the RS principle, the communication message is split into a robust stream and a supplementary stream in order to enable more flexible interference management between communication and sensing [3], [16]. These streams are superimposed with a deterministic radar sequence known *a priori* at the BS, thereby enabling coherent sensing [3], [27]. The transmitted frequency-domain symbol on subcarrier n and OFDM symbol m is

$$X_n[m] = \sqrt{p_{c,1}[n]} s_{c,1}[n, m] + \sqrt{p_{c,2}[n]} s_{c,2}[n, m] + \sqrt{p_r[n]} s_r[n, m], \quad (1)$$

where $s_{c,1}[n, m]$ and $s_{c,2}[n, m]$ denote the information symbols of the two communication streams, respectively, and $s_r[n, m]$ denotes the deterministic radar symbol. The communication symbols are modeled as zero-mean and unit-power, i.e., $\mathbb{E}\{s_{c,i}[n, m]\} = 0$ and $\mathbb{E}\{|s_{c,i}[n, m]|^2\} = 1$ for $i \in \{1, 2\}$, while $s_r[n, m]$ is a unit-power deterministic sequence. The non-negative coefficients $p_{c,1}[n]$, $p_{c,2}[n]$, and $p_r[n]$ denote the power allocated to each component on subcarrier n and satisfy the per-OFDM-symbol transmit power constraint

$$\sum_{n \in \mathcal{N}} (p_{c,1}[n] + p_{c,2}[n] + p_r[n]) \leq P_{tx}, \quad (2)$$

where P_{tx} is the maximum transmit power per OFDM symbol at the UE. The resulting non-orthogonal superposition follows the power-domain signal structuring principle underlying RSMA frameworks [15]–[17], [28]–[30].

Let $\mathbf{x}[m] \triangleq [X_0[m], \dots, X_{N_{sc}-1}[m]]^T \in \mathbb{C}^{N_{sc} \times 1}$ denote the frequency-domain transmit vector at time index m . Assuming that the cyclic prefix length is sufficient to cover the effective delay spread, the corresponding time-domain (TD) transmit block is obtained via a unitary inverse fast Fourier transform (IFFT) followed by cyclic prefix (CP) insertion

$$\mathbf{x}_{tx,TD}[m] = \mathbf{A}\mathbf{F}^H \mathbf{x}[m] \in \mathbb{C}^{(N_{sc}+N_{cp}) \times 1}, \quad (3)$$

where $\mathbf{F} \in \mathbb{C}^{N_{sc} \times N_{sc}}$ denotes the unitary fast Fourier transform (FFT) matrix and $\mathbf{A} \in \mathbb{R}^{(N_{sc} + N_{cp}) \times N_{sc}}$ appends a CP of length N_{cp} [17]. Specifically,

$$\mathbf{A} = \begin{bmatrix} \mathbf{0}_{N_{cp} \times (N_{sc} - N_{cp})} & \mathbf{I}_{N_{cp}} \\ & \mathbf{I}_{N_{sc}} \end{bmatrix}. \quad (4)$$

B. DP Signal Model (UE \rightarrow BS)

In discrete time, the DP channel during the m -th OFDM symbol is represented as [17]

$$\mathbf{H}_{\text{TD}}^{(\text{DP})}[m] = \sum_{l=1}^L \alpha_l \mathbf{\Pi}^{n_{\tau_l}} \mathbf{\Delta}(\nu_l), \quad (5)$$

where $n_{\tau_l} = \lfloor \tau_l / T_s \rfloor$ denotes the discrete delay index with T_s the sampling period, $\mathbf{\Pi}$ is the cyclic delay-shift matrix, and $\mathbf{\Delta}(\nu_l)$ is a diagonal Doppler operator defined as

$$\mathbf{\Delta}(\nu_l) = \text{diag} \left(\left[1, e^{j2\pi\nu_l \frac{1}{F_s}}, \dots, e^{j2\pi\nu_l \frac{N_{sc} + N_{cp} - 1}{F_s}} \right]^T \right), \quad (6)$$

with $F_s \triangleq 1/T_s$ denoting the sampling frequency [17]. The noiseless TD received block due to the DP at the BS is then

$$\mathbf{y}_{\text{rx,TD}}^{(\text{DP})}[m] = \mathbf{H}_{\text{TD}}^{(\text{DP})}[m] \mathbf{x}_{\text{tx,TD}}[m]. \quad (7)$$

At the receiver, the CP is removed by $\mathbf{B} = [\mathbf{0}_{N_{sc} \times N_{cp}} \quad \mathbf{I}_{N_{sc}}]$, and the signal is transformed to the frequency-domain (FD) through the FFT matrix \mathbf{F} . The resulting effective FD channel matrix is [17]

$$\mathbf{H}_{\text{FD}}^{(\text{DP})}[m] \triangleq \mathbf{F} \mathbf{B} \mathbf{H}_{\text{TD}}^{(\text{DP})}[m] \mathbf{A} \mathbf{F}^H, \quad (8)$$

so that the DP component of the received FD vector is

$$\mathbf{y}_{\text{rx,FD}}^{(\text{DP})}[m] = \mathbf{H}_{\text{FD}}^{(\text{DP})}[m] \mathbf{x}[m]. \quad (9)$$

Equivalently, on subcarrier n ,

$$y_{\text{rx,FD},n}^{(\text{DP})}[m] = \sum_{k \in \mathcal{N}} H_{\text{FD},n,k}^{(\text{DP})}[m] X_k[m], \quad (10)$$

where $H_{\text{FD},n,n}^{(\text{DP})}[m]$ denotes the desired subcarrier gain, while the off-diagonal terms model Doppler-induced ICI leakage from subcarrier k to n [12], [14], [17]. Since the receiver is synchronized to the dominant DP LoS component [11], the common UE-BS Doppler shift can be compensated, largely restoring subcarrier orthogonality on the direct path. Accordingly, we model $\mathbf{H}_{\text{FD}}^{(\text{DP})}[m]$ as diagonal,¹ i.e., the residual off-diagonal ICI terms in (10) are neglected for the direct path. In contrast, the Doppler shifts of the target echoes remain uncompensated, so the impact of mobility is transferred to the sensing stage, where it manifests as ICI in the EP channel.

C. Bistatic EP Signal Model (UE \rightarrow Target \rightarrow BS)

The BS also receives a target-reflected bistatic echo. For analytical tractability, we model the echo channel by a single dominant bistatic path with complex gain α_R . Its squared magnitude is modelled according to the bistatic radar equation

$$|\alpha_R|^2 = \frac{G_{\text{UE}} G_{\text{BS}} \lambda^2 \sigma_{\text{RCS}}^{\text{bi}}}{(4\pi)^3 R_{\text{UT}}^2 R_{\text{TB}}^2}, \quad (11)$$

¹This diagonalization is adopted for the direct path only, under dominant-LoS synchronization, and any residual direct-path ICI is neglected relative to the uncompensated echo-path ICI considered subsequently [11], [12].

where G_{UE} and G_{BS} denote the effective antenna gains, λ is the wavelength, $\sigma_{\text{RCS}}^{\text{bi}}$ is the bistatic radar cross-section (RCS), and R_{UT} and R_{TB} are the UE-to-target and target-to-BS ranges, respectively [31]. The phase of α_R is modelled as uniformly distributed over $[0, 2\pi)$. The corresponding bistatic propagation delay is

$$\tau_{\text{tar}} = \frac{R_{\text{UT}} + R_{\text{TB}}}{c}, \quad (12)$$

where c denotes the speed of light.

Since the BS is synchronized to the strong DP signal for communication decoding [11], the direct-path Doppler component is effectively compensated at the receiver. Consequently, the echo is observed with a residual Doppler shift given by

$$\nu_{\text{tar}} = \nu_{\text{abs}} - \nu_{\text{DP}}. \quad (13)$$

where ν_{abs} denotes the absolute bistatic Doppler associated with the target-reflected path, and ν_{DP} is the compensated Doppler of the direct path. Based on the geometry in Fig. 1, the absolute bistatic Doppler is given by [26]

$$\nu_{\text{abs}} = \frac{\|\mathbf{v}_{\text{UE}}\|}{\lambda} \cos(\delta_{\text{tx}}) + \frac{2\|\mathbf{v}_{\text{tar}}\|}{\lambda} \cos \phi \cos(\beta/2), \quad (14)$$

while the direct-path Doppler is

$$\nu_{\text{DP}} = \frac{\|\mathbf{v}_{\text{UE}}\|}{\lambda} \cos(\delta_{\text{tx}} + \theta_T), \quad (15)$$

where \mathbf{v}_{tar} and \mathbf{v}_{UE} denote the target and UE velocity vectors, δ_{tx} is the angle of the UE velocity relative to the illumination path, θ_T is the angle between the illumination path and the direct path, and ϕ is the angle defining the target-velocity projection in the bistatic geometry. Using the same delay and Doppler operators as in the direct-path model, the echo channel matrix in the time domain is

$$\mathbf{H}_{\text{TD}}^{(\text{EP})}[m] = \alpha_R \mathbf{\Pi}^{n_{\tau_{\text{tar}}}} \mathbf{\Delta}(\nu_{\text{tar}}), \quad (16)$$

with $n_{\tau_{\text{tar}}} = \lfloor \tau_{\text{tar}} / T_s \rfloor$. After CP removal and FFT, the corresponding effective echo channel in the FD is

$$\mathbf{H}_{\text{FD}}^{(\text{EP})}[m] \triangleq \mathbf{F} \mathbf{B} \mathbf{H}_{\text{TD}}^{(\text{EP})}[m] \mathbf{A} \mathbf{F}^H. \quad (17)$$

Hence, the echo component of the received FD vector is

$$\mathbf{y}_{\text{rx,FD}}^{(\text{EP})}[m] = \mathbf{H}_{\text{FD}}^{(\text{EP})}[m] \mathbf{x}[m]. \quad (18)$$

On subcarrier n , this becomes

$$y_{\text{rx,FD},n}^{(\text{EP})}[m] = \underbrace{H_{\text{FD},n,n}^{(\text{EP})}[m] X_n[m]}_{\text{Target Return}} + \underbrace{\sum_{k \in \mathcal{N}, k \neq n} H_{\text{FD},n,k}^{(\text{EP})}[m] X_k[m]}_{\text{Doppler-induced Echo ICI}}. \quad (19)$$

where the diagonal term captures the phase rotation induced by τ_{tar} and ν_{tar} , while the off-diagonal terms represent Doppler-induced leakage across subcarriers. This loss of orthogonality follows the well-known Dirichlet-kernel structure as a function of the normalized residual Doppler $\nu_{\text{tar}} / \Delta f$ [11], [32].

D. Total Received Signal and Receiver-Related Assumptions

We assume symbol-level synchronization at the BS such that the DP and EP arrivals lie within the CP window, as supported

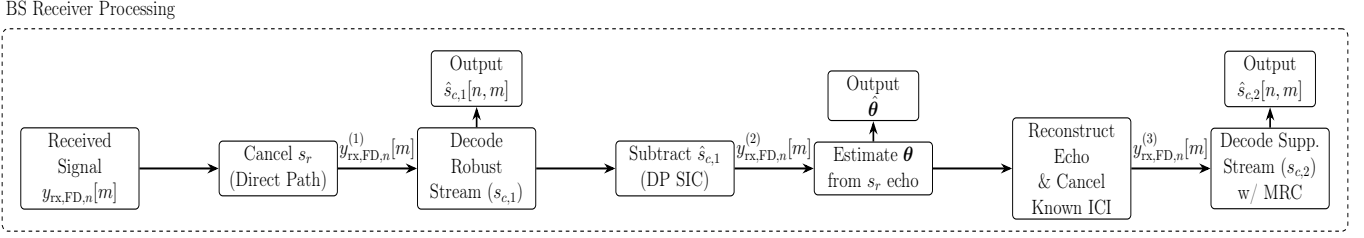


Figure 2: Proposed RS-inspired staged receiver at the BS: the DP radar sequence is cancelled, the robust stream ($s_{c,1}$) is decoded and subtracted via SIC, target parameters ($\tau_{\text{tar}}, \nu_{\text{tar}}$) are estimated from the residual, and the reconstructed echo is used to suppress ICI before maximum-ratio combining (MRC) decoding of the supplementary stream ($s_{c,2}$).

by closed-loop timing advance in uplink systems [24], [33]. The received FD signal on subcarrier n is

$$y_{\text{rx,FD},n}[m] = y_{\text{rx,FD},n}^{\text{(DP)}}[m] + y_{\text{rx,FD},n}^{\text{(EP)}}[m] + z_{\text{BS,FD},n}[m], \quad (20)$$

where $z_{\text{BS,FD},n}[m] \sim \mathcal{CN}(0, \sigma_{\text{BS}}^2)$ denotes additive white gaussian noise (AWGN) with variance σ_{BS}^2 .

We adopt a blockwise channel state information (CSI)-aware rate-adaptation model. At the beginning of each transmission block, the BS acquires an estimate of the DP CSI $H_{\text{DP},n}[m]$, uses it to compute the blockwise power allocation signalled to the UE, and, in the subsequent data-reception phase, uses the same CSI, together with the known $s_r[n, m]$, to cancel the DP radar component, analogous to direct-blast suppression in bistatic/passive radar [26], [34] and interference cancellation in full-duplex systems [35]. The same DP CSI is then used for robust-stream decoding. Accordingly, the reported SE expressions are conditioned on CSI acquisition and abstract from the associated training/feedback overhead, which is common to all schemes and thus does not affect the relative comparison. Finally, we adopt a single-input single-output (SISO)-equivalent baseline under beam alignment, so that array effects are absorbed into the effective link budget.

III. RECEIVER PROCESSING AND SINR ANALYSIS

To recover the superposed waveform in (1) from the received signal model in (20), we employ the staged receiver illustrated in Fig. 2. The processing order follows the RS-inspired principle in [3]: i) cancel the known direct-path radar component; ii) decode the robust stream $s_{c,1}$ and remove it via SIC; iii) estimate the target parameters using the known radar reference s_r and reconstruct the echo-path component; and iv) cancel the reconstructed echo and decode the supplementary stream $s_{c,2}$. Subsequently, to derive tractable per-subcarrier SINR expressions, we adopt the DP/EP channel structure established in Section II. In particular, the DP is modelled as diagonal after synchronization to the dominant DP LoS component, so that residual DP ICI is neglected. By contrast, the EP remains affected by residual bistatic Doppler and fractional delay, which destroy subcarrier orthogonality and induce ICI [17].

Let $\xi_{n,k}(\nu_{\text{tar}})$ denote the EP power leakage coefficient from subcarrier k to subcarrier n , with $\xi_{n,n}$ representing the desired intra-carrier power coefficient. By treating the resulting uncorrelated interference and ICI terms as Gaussian noise

[17], detection can be decoupled across subcarriers, yielding closed-form per-subcarrier SINR expressions.

a) Step 1: DP Radar Interference Cancellation: Using the known radar sequence $s_r[n, m]$ and the DP FD channel coefficients $H_{\text{DP},n}[m]$, the BS removes the DP replica of the radar component from the received signal [27]. Under the assumption of perfect DP radar cancellation, the post-cancellation signal on subcarrier n is

$$\begin{aligned} y_{\text{rx,FD},n}^{(1)}[m] &= y_{\text{rx,FD},n}[m] - H_{\text{DP},n}[m] \sqrt{p_r[n]} s_r[n, m] \\ &= \tilde{y}_{\text{rx,FD},n}^{(\text{DP},c)}[m] + y_{\text{rx,FD},n}^{\text{(EP)}}[m] + z_{\text{BS,FD},n}[m], \end{aligned} \quad (21)$$

where $\tilde{y}_{\text{rx,FD},n}^{(\text{DP},c)}[m]$ contains only the DP contributions of the communication streams:

$$\begin{aligned} \tilde{y}_{\text{rx,FD},n}^{(\text{DP},c)}[m] &= H_{\text{DP},n}[m] \left(\sqrt{p_{c,1}[n]} s_{c,1}[n, m] \right. \\ &\quad \left. + \sqrt{p_{c,2}[n]} s_{c,2}[n, m] \right). \end{aligned} \quad (22)$$

This operation cancels only the DP radar replica, since the EP term propagates through the distinct bistatic channel $\mathbf{H}_{\text{FD}}^{(\text{EP})}[m]$ and therefore is not matched by a replica constructed from $H_{\text{DP},n}[m]$ [26], [34].

b) Step 2: Decoding of the Robust Stream ($s_{c,1}$): The BS decodes $s_{c,1}[n, m]$ from $y_{\text{rx,FD},n}^{(1)}[m]$ using a DP-matched detector, following the RS decoding order in [3]. At this stage, the supplementary stream $s_{c,2}$ acts as the dominant DP interferer. Since the echo channel has not yet been estimated, the entire EP contribution, including both intra-carrier and inter-carrier terms, is treated as residual interference. The desired signal power on subcarrier n is therefore

$$S_{c,1,n} = |H_{\text{DP},n}[m]|^2 p_{c,1}[n]. \quad (23)$$

To capture the Doppler-induced leakage over the echo path, let $\xi_{n,k}(\nu_{\text{tar}})$ denote the power leakage coefficient from subcarrier k to subcarrier n . Using the standard Dirichlet-kernel-based OFDM ICI model [36], we write

$$\xi_{n,k}(\nu_{\text{tar}}) = \left| \frac{\sin(\pi(k-n+\nu_{\text{tar}}/\Delta f))}{N_{\text{sc}} \sin(\frac{\pi}{N_{\text{sc}}}(k-n+\nu_{\text{tar}}/\Delta f))} \right|^2, \quad (24)$$

where Δf is the subcarrier spacing. Let $H_{\text{EP},k}[m]$ denote the effective EP coefficient associated with subcarrier k . The

aggregate interference power is then approximated as

$$I_{c,1,n} = \underbrace{|H_{DP,n}[m]|^2 p_{c,2}[n]}_{\text{DP interference from } s_{c,2}} + \underbrace{\sum_{k \in \mathcal{N}} \xi_{n,k} |H_{EP,k}[m]|^2 (p_{c,1}[k] + p_{c,2}[k] + p_r[k])}_{\text{Total Echo Clutter \& ICI (Radar + Comm)}}, \quad (25)$$

leading to the per-subcarrier SINR

$$\gamma_{c,1,n} = \frac{S_{c,1,n}}{I_{c,1,n} + \sigma_{BS}^2}. \quad (26)$$

Thus, the robust stream is affected by both the supplementary stream on the strong direct path and the uncancelled EP interference. Upon successful decoding, the BS regenerates $\hat{s}_{c,1}$ and subtracts its DP contribution via SIC.

c) Step 3: Target Parameter Estimation: After decoding $s_{c,1}$ in Step 2, the BS regenerates $\hat{s}_{c,1}[n, m]$ and cancels its DP contribution using $H_{DP,n}[m]$. The resulting residual signal is then used for sensing. In particular, the target parameters $\theta = [\tau_{tar}, \nu_{tar}]$ are estimated using the sequence $s_r[n, m]$ through matched filtering [37]. Let $H_{EP,n}[m]$ denote the effective intra-carrier echo-path coefficient on subcarrier n . The desired per-subcarrier radar signal power is then

$$S_{r,n} = \xi_{n,n} |H_{EP,n}[m]|^2 p_r[n]. \quad (27)$$

At this stage, the interference consists of three components: i) the DP contribution of the not-yet-decoded stream $s_{c,2}$, ii) the EP contributions of the communication streams, and iii) radar self-ICI arising from the leakage of the radar sequence from subcarriers $k \neq n$. Accordingly, the aggregate interference power is

$$I_{r,n} = \underbrace{|H_{DP,n}[m]|^2 p_{c,2}[n]}_{\text{direct-path interference from } s_{c,2}} + \underbrace{\sum_{k \in \mathcal{N}} \xi_{n,k} |H_{EP,k}[m]|^2 (p_{c,1}[k] + p_{c,2}[k])}_{\text{echo-path communication interference and ICI}} + \underbrace{\sum_{k \neq n} \xi_{n,k} |H_{EP,k}[m]|^2 p_r[k]}_{\text{radar self-ICI}}, \quad (28)$$

leading to the per-subcarrier sensing SINR

$$\gamma_{r,n} = \frac{S_{r,n}}{I_{r,n} + \sigma_{BS}^2}. \quad (29)$$

d) Step 4: Decoding of the Supplementary Stream ($s_{c,2}$): Using $\hat{\theta} = [\hat{\tau}_{tar}, \hat{\nu}_{tar}]$ from Step 3, the BS reconstructs the echo-path channel response. Unlike the decoding of $s_{c,1}$, the decoding of $s_{c,2}$ exploits both the DP component and the reconstructed EP component of the supplementary stream through coherent combining, thereby increasing the effective received signal power [38, Ch. 3]. However, estimation errors $\Delta\theta$ lead to imperfect echo-channel and ICI reconstruction. Under a high-signal-to-noise ratio (SNR) approximation, the parameter error variance approaches the CRLB [37]. Applying a first-order Taylor expansion and the delta method [39], [40],

the resulting residual EP mismatch power is modeled as

$$P_{\text{mismatch},n} = \sigma_{e,n}^2[m] \left(\sum_{k \in \mathcal{N}} \xi_{n,k} (p_{c,1}[k] + p_r[k] + p_{c,2}[n]) \right), \quad (30)$$

where $\sigma_{e,n}^2[m]$ denotes the variance of the echo-channel reconstruction error. This term captures the residual error arising from imperfect cancellation of the known EP components associated with $s_{c,1}$ and s_r , as well as imperfect coherent combining of the desired EP component of $s_{c,2}[n]$. Crucially, because the supplementary-stream symbols on the other subcarriers ($k \neq n$) are not yet known, their EP ICI cannot be reconstructed or cancelled and therefore remains as uncancelled interference. The post-processing SINR for $s_{c,2}$ is thus given by

$$\gamma_{c,2,n} = \frac{|H_{DP,n}[m] + \hat{H}_{EP,n}[m]|^2 p_{c,2}[n]}{P_{\text{mismatch},n} + \sum_{k \neq n} \xi_{n,k} |H_{EP,k}[m]|^2 p_{c,2}[k] + \sigma_{BS}^2}. \quad (31)$$

Equation (31) highlights the central sensing–communication coupling in the proposed architecture. Increasing the supplementary-stream power $p_{c,2}$ strengthens the desired signal term, but it also degrades the sensing stage in Step 3 through a larger interference term $I_{r,n}$. The resulting deterioration in estimation accuracy increases $P_{\text{mismatch},n}$, while the uncancelled supplementary-stream ICI in the denominator also scales with $p_{c,2}$. This yields a non-convex trade-off that motivates the joint power-allocation framework developed later.

A. Estimation Accuracy and CRLB Analysis

We quantify sensing accuracy through the CRLB of the target delay–Doppler parameters $\theta = [\tau_{tar}, \nu_{tar}]^T$, and later relate this estimation accuracy to the residual echo-channel reconstruction error that limits communication decoding. The error covariance of any unbiased estimator is lower-bounded by the inverse of the fisher information matrix (FIM) $\mathbf{J}(\theta)$ [41]. Under the Gaussian approximation adopted in the preceding SINR analysis, the (i, j) -th FIM entry for the discrete-time OFDM signal model is given by [37]

$$[\mathbf{J}(\theta)]_{i,j} = 2 \text{Re} \left\{ \sum_{n \in \mathcal{N}} \sum_{m=0}^{M-1} \frac{1}{\sigma_{in,n}^2} \left(\frac{\partial \tilde{s}_{r,n}^*[m]}{\partial \theta_i} \frac{\partial \tilde{s}_{r,n}[m]}{\partial \theta_j} \right) \right\}, \quad (32)$$

where $\tilde{s}_{r,n}[m]$ denotes the noise-free desired EP radar component on subcarrier n and symbol m , and $\sigma_{in,n}^2 \triangleq I_{r,n} + \sigma_{BS}^2$ is the corresponding interference-plus-noise power. In OFDM, the parameter information is embedded in the phase

$$\phi_{n,m} = 2\pi(n\Delta f \tau_{tar} + mT_{\text{sym}}\nu_{tar}),$$

where T_{sym} denotes the OFDM symbol duration used in the delay–Doppler phase model. Following [41], [42], the derivatives of the echo phase with respect to delay and Doppler are proportional to the subcarrier index n and symbol index m , respectively. Substituting these derivatives into (32), the FIM can be expressed compactly in terms of the per-subcarrier sensing SINR $\gamma_{r,n}$ as

$$\mathbf{J}(\theta) = \begin{bmatrix} K_{\tau\tau} \sum_{n \in \mathcal{N}} n^2 \gamma_{r,n} & K_{\tau\nu} \sum_{n \in \mathcal{N}} n \gamma_{r,n} \\ K_{\tau\nu} \sum_{n \in \mathcal{N}} n \gamma_{r,n} & K_{\nu\nu} \sum_{n \in \mathcal{N}} \gamma_{r,n} \end{bmatrix}. \quad (33)$$

where the subcarrier-independent kernel constants, which encapsulate the waveform parameters (bandwidth and duration), are expressed as [41]:

$$\begin{bmatrix} K_{\tau\tau} \\ K_{\nu\nu} \\ K_{\tau\nu} \end{bmatrix} = 8\pi^2 \begin{bmatrix} (\Delta f)^2 M \\ (T_{\text{sym}})^2 \sum_{m=0}^{M-1} m^2 \\ (\Delta f T_{\text{sym}}) \sum_{m=0}^{M-1} m \end{bmatrix}. \quad (34)$$

B. Channel Reconstruction Error Analysis

To quantify the impact of sensing uncertainty on communication decoding, we map the parameter estimation error covariance $\mathbf{J}^{-1}(\boldsymbol{\theta})$ obtained in Section III-A to the echo-channel reconstruction error variance $\sigma_{e,n}^2[m]$, which later determines the residual term in (30). We assume that the path gain α_R is perfectly tracked, so that the reconstruction error arises solely from uncertainty in the delay–Doppler parameters. The reconstructed echo-channel response at subcarrier n and symbol m is parameterized by $\boldsymbol{\theta} = [\tau, \nu]^T$ as

$$H_{\text{EP},n}[m; \boldsymbol{\theta}] = \alpha_R \exp(-j2\pi n \Delta f \tau) \exp(+j2\pi m T_{\text{sym}} \nu), \quad (35)$$

For small estimation errors $\Delta\boldsymbol{\theta} = \boldsymbol{\theta} - \hat{\boldsymbol{\theta}}$, a first-order Taylor expansion yields [39], [40]

$$e_n[m] \approx \nabla_{\boldsymbol{\theta}} H_{\text{EP},n}[m]^T \cdot \Delta\boldsymbol{\theta}, \quad (36)$$

where

$$\nabla_{\boldsymbol{\theta}} H_{\text{EP},n}[m] = \left[\frac{\partial H_{\text{EP},n}[m]}{\partial \tau}, \frac{\partial H_{\text{EP},n}[m]}{\partial \nu} \right]^T.$$

is the gradient vector. Consequently, the variance of the channel estimation error is given by the quadratic form

$$\sigma_{e,n}^2[m] = \nabla_{\boldsymbol{\theta}} H_{\text{EP},n}[m]^H \mathbf{J}^{-1}(\boldsymbol{\theta}) \nabla_{\boldsymbol{\theta}} H_{\text{EP},n}[m]. \quad (37)$$

Evaluating the partial derivatives of the phase terms in (35), we obtain

$$\frac{\partial H_{\text{EP}}}{\partial \tau} = (-j2\pi n \Delta f) \cdot H_{\text{EP},n}[m], \quad (38)$$

$$\frac{\partial H_{\text{EP}}}{\partial \nu} = (+j2\pi m T_{\text{sym}}) \cdot H_{\text{EP},n}[m]. \quad (39)$$

Substituting these derivatives into (37) and factoring out the channel magnitude $|H_{\text{EP},n}[m]|^2 = |\alpha_R|^2$, we arrive at the closed-form expression for the error variance:

$$\sigma_{e,n}^2[m] = |\alpha_R|^2 \cdot \Omega[n, m], \quad (40)$$

where $\Omega[n, m]$ is the normalized frequency–time sensitivity factor. Letting $C_{xy} \triangleq [\mathbf{J}^{-1}(\mathbf{p})]_{xy}$ denote the elements of the inverse FIM (representing the variance and covariance of the estimation errors), $\Omega[n, m]$ is given by:

$$\Omega[n, m] = 4\pi^2 \left(C_{\tau\tau} (n\Delta f)^2 + C_{\nu\nu} (mT_{\text{sym}})^2 - 2C_{\tau\nu} (n\Delta f)(mT_{\text{sym}}) \right). \quad (41)$$

This expression explicitly shows that the echo-channel reconstruction error is non-uniform across the OFDM grid: subcarriers with larger absolute indices $|n|$ are more sensitive to delay-estimation errors, while later symbols are more sensitive to Doppler-estimation errors.

IV. OPTIMIZATION AND PROPOSED SOLUTION

To maximize communication throughput while guaranteeing sensing accuracy, we design the per-subcarrier power allocation of the proposed RS-inspired superposition signal under a sensing-performance constraint. Let $\mathbf{p}_{c,1}$, $\mathbf{p}_{c,2}$, and $\mathbf{p}_r \in \mathbb{R}_+^{N_{\text{sc}}}$ collect the powers allocated across subcarriers to the robust stream, the supplementary stream, and the radar sequence, respectively, and define $\mathbf{p} \triangleq (\mathbf{p}_{c,1}, \mathbf{p}_{c,2}, \mathbf{p}_r)$. Subsequently, the aggregate communication SE is

$$R_{\text{sum}}(\mathbf{p}) = \sum_{n \in \mathcal{N}} \log_2((1 + \gamma_{c,1,n})(1 + \gamma_{c,2,n})), \quad (42)$$

where $\gamma_{c,1,n}(\mathbf{p})$ and $\gamma_{c,2,n}(\mathbf{p})$ are given in Section III.

Sensing performance is quantified through the weighted A-optimal CRLB criterion

$$\text{Tr}(\mathbf{W}\mathbf{J}^{-1}(\mathbf{p})),$$

where $\mathbf{J}(\mathbf{p})$ is the FIM associated with $\boldsymbol{\theta} = [\tau_{\text{tar}}, \nu_{\text{tar}}]^T$ (cf. Section III-A), and $\mathbf{W} = \text{diag}(w_\tau, w_\nu)$ is a diagonal weighting matrix. Following [43], we set $w_\tau = (c/2)^2$ and $w_\nu = (\lambda/2)^2$ so that delay and Doppler errors are measured in consistent physical units of range and velocity, respectively. Since $\mathbf{J}(\mathbf{p})$ depends on the sensing SINR, while the same power variables also determine $R_{\text{sum}}(\mathbf{p})$, the design is inherently coupled. We therefore formulate the following sensing-constrained joint power-allocation problem:

$$\max_{\mathbf{p}} R_{\text{sum}}(\mathbf{p}) \quad (43a)$$

$$\text{s.t. } \text{Tr}(\mathbf{W}\mathbf{J}^{-1}(\mathbf{p})) \leq \Gamma_{\text{sens}}, \quad (43b)$$

$$\sum_{n \in \mathcal{N}} (p_{c,1}[n] + p_{c,2}[n] + p_r[n]) \leq P_{\text{tx}}, \quad (43c)$$

$$P_{\text{min}} \leq p_{c,1}[n] + p_{c,2}[n] + p_r[n] \leq P_{\text{max}}, \quad \forall n \in \mathcal{N}, \quad (43d)$$

$$p_{c,1}[n] \geq 0, p_{c,2}[n] \geq 0, p_r[n] \geq 0, \quad \forall n \in \mathcal{N}. \quad (43e)$$

Here, Γ_{sens} denotes the maximum tolerable weighted sensing error, and P_{tx} is the transmit power budget per OFDM symbol. Constraint (43d) optionally imposes a per-subcarrier power tube to avoid excessively uneven spectral allocations; when such a constraint is not required, it can be relaxed by setting $P_{\text{min}} = 0$ and $P_{\text{max}} = P_{\text{tx}}$, or omitted altogether.

Problem (43) is intractable due to: i) the nonconcave objective (43a), which contains logarithms of fractional SINR expressions; and ii) the inverse FIM $\mathbf{J}^{-1}(\mathbf{p})$ in the sensing constraint, together with its implicit appearance in the mismatch term affecting $\gamma_{c,2,n}(\mathbf{p})$. In the following, we address these two difficulties to obtain a tractable reformulation.

A. A-Optimal Design and Surrogate Reformulation

The tractable reformulation proceeds in two steps. First, the weighted A-optimal sensing constraint is recast through an LMI-based surrogate. Second, the mismatch term induced by echo-channel reconstruction error is approximated by a convex ICI-aware surrogate.

a) *A-Optimal CRLB surrogate via an LMI*: Following A-optimal experiment design [44], we introduce a symmetric

matrix $\mathbf{X} \in \mathbb{S}_+^2$ satisfying $\mathbf{X} \succeq \mathbf{J}^{-1}(\mathbf{p})$, so that the weighted sensing constraint can be conservatively enforced through $\text{Tr}(\mathbf{W}\mathbf{X}) \leq \Gamma_{\text{sens}}$. To decouple the FIM from the fractional sensing SINR terms, we introduce auxiliary variables $\mathbf{z} = [z_0, \dots, z_{N_{\text{sc}}-1}]^T$ satisfying $0 \leq z_n \leq \gamma_{r,n}(\mathbf{p})$ for all $n \in \mathcal{N}$. Since the FIM is affine in the per-subcarrier sensing SINR, we define the surrogate

$$\mathbf{J}(\mathbf{z}) \triangleq \sum_{n \in \mathcal{N}} z_n \mathbf{K}_n, \quad (44)$$

where \mathbf{K}_n denotes the per-subcarrier Fisher-information base matrix induced by the compact form in (33). To ensure invertibility and numerical stability, we impose $\mathbf{J}(\mathbf{z}) \succeq \delta \mathbf{I}_2$ for a small $\delta > 0$. Then, by the Schur complement lemma [44],

$$\begin{bmatrix} \mathbf{X} & \mathbf{I}_2 \\ \mathbf{I}_2 & \mathbf{J}(\mathbf{z}) \end{bmatrix} \succeq 0 \implies \mathbf{X} \succeq \mathbf{J}(\mathbf{z})^{-1}. \quad (45)$$

b) Convex ICI-aware surrogate for the mismatch sensitivity: The residual mismatch term in $\gamma_{c,2,n}$ depends on the delay-Doppler error covariance $\mathbf{C} \triangleq \mathbf{J}^{-1}(\mathbf{p})$, with entries $C_{\tau\tau}$, $C_{\nu\nu}$, and $C_{\tau\nu}$. Since $\mathbf{X} \succeq \mathbf{J}(\mathbf{z})^{-1}$, the diagonal entries satisfy $X_{11} \geq C_{\tau\tau}$ and $X_{22} \geq C_{\nu\nu}$. For the off-diagonal term, positive semi-definite (PSD) ordering implies $|C_{\tau\nu}| \leq \sqrt{C_{\tau\tau}C_{\nu\nu}}$, which is further upper-bounded via the arithmetic-geometric mean inequality as

$$|C_{\tau\nu}| \leq \frac{1}{2}(\beta C_{\tau\tau} + \beta^{-1} C_{\nu\nu}) \leq \frac{1}{2}(\beta X_{11} + \beta^{-1} X_{22}). \quad (46)$$

where $\beta > 0$ is a scaling parameter used to preserve physical consistency between delay and Doppler units. Using $a_n \triangleq n\Delta f$ and $b_m \triangleq mT_{\text{sym}}$, the normalized sensitivity factor

$$\Omega[n, m] = 4\pi^2(C_{\tau\tau}a_n^2 + C_{\nu\nu}b_m^2 - 2C_{\tau\nu}a_nb_m)$$

admits the conservative affine upper bound

$$\tilde{\Omega}[n, m; \mathbf{X}] \triangleq 4\pi^2 \left(X_{11}a_n^2 + X_{22}b_m^2 + (\beta X_{11} + \beta^{-1} X_{22}) |a_nb_m| \right), \quad (47)$$

which avoids introducing an additional auxiliary variable for the off-diagonal term. Let $\sigma_{e,n}^2(\mathbf{X}) \triangleq |\alpha_R|^2 \tilde{\Omega}[n, m; \mathbf{X}]$ denote the resulting convex surrogate for the echo-channel reconstruction error variance, averaged over the symbol indices m to capture the block-wide effect.

To reflect that Doppler-induced ICI spreads the echo energy across subcarriers, the residual power after echo reconstruction/cancellation of the *known* components (s_r and the decoded $s_{c,1}$) on bin n is modeled through the leakage coefficients $\xi_{n,k}$. Accordingly, we define the ICI-aware effective energy term

$$t_n(\mathbf{p}) \triangleq \sum_{k \in \mathcal{N}} \xi_{n,k} (p_{c,1}[k] + p_r[k]) + p_{c,2}[n] \geq 0, \quad (48)$$

where the first term captures residual echo leakage from the *known* waveforms across all subcarriers and the second term accounts for the supplementary-stream self-noise on the target bin when the reconstructed echo is used for coherent combining.

Substituting into (30) yields a bilinear mismatch term $\sigma_{e,n}^2(\mathbf{X}) t_n(\mathbf{p})$, where the sensing matrix surrogate \mathbf{X} and the power allocation \mathbf{p} appear as factors belonging to distinct block coordinate descent (BCD) blocks. To handle this non-convexity

while preserving the coupling between the two blocks, we linearize the bilinear product via a first-order Taylor expansion [45], a standard successive convex approximation (SCA) strategy for decoupling multiplicatively coupled variables in iterative optimization. Let $\sigma_{e,n}^{2,(i)}$ and $t_n^{(i)}$ denote the values of the mismatch variance and the effective ICI-aware energy evaluated at the previous BCD iteration, respectively. The bilinear product is then approximated by its affine surrogate:

$$\sigma_{e,n}^2(\mathbf{X}) t_n(\mathbf{p}) \approx \sigma_{e,n}^{2,(i)} t_n(\mathbf{p}) + t_n^{(i)} \sigma_{e,n}^2(\mathbf{X}) - \sigma_{e,n}^{2,(i)} t_n^{(i)}, \quad (49)$$

which defines the linear mismatch surrogate. It is worth noting that this linearization serves exclusively as a convex surrogate within the optimization procedure; all SINR expressions in Section V are evaluated using the exact reconstruction error variance $\sigma_{e,n}^2[m]$ from (40).

$$\tilde{P}_{\text{mismatch},n}(\mathbf{p}, \mathbf{X}) \triangleq \sigma_{e,n}^{2,(i)} t_n(\mathbf{p}) + t_n^{(i)} \sigma_{e,n}^2(\mathbf{X}) - \sigma_{e,n}^{2,(i)} t_n^{(i)}. \quad (50)$$

In the proposed alternating procedure, the reference points $\sigma_{e,n}^{2,(i)}$ and $t_n^{(i)}$ are treated as fixed constants within each convex subproblem and are iteratively updated using the solutions from the previous iteration, ensuring convergence to a stationary point of the original non-convex design.

B. Fractional Programming and Dual Transformations

To handle the remaining non-convexity in the communication objective function (43a) and the sensing epigraph constraints $z_n \leq \gamma_{r,n}(\mathbf{p})$, we leverage the multidimensional fractional programming (FP) framework [45]. The key idea is to introduce auxiliary variables that yield tight concave surrogate expressions, enabling an alternating optimization (AO) procedure.

a) Lagrangian dual transform for the log-sum-rate:

For each stream $i \in \{1, 2\}$ and subcarrier n , we apply the Lagrangian dual transform [45] by introducing auxiliary variables $\alpha_{c,i,n} \geq 0$:

$$\begin{aligned} \log_2(1 + \gamma_{c,i,n}) &= \max_{\alpha_{c,i,n} \geq 0} \log_2(1 + \alpha_{c,i,n}) - \alpha_{c,i,n} \log_2 e \\ &\quad + \frac{(1 + \alpha_{c,i,n}) \gamma_{c,i,n}}{1 + \gamma_{c,i,n}} \log_2 e. \end{aligned} \quad (51)$$

The maximizer satisfies $\alpha_{c,i,n}^* = \gamma_{c,i,n}$. Noting that $\gamma_{c,i,n}/(1 + \gamma_{c,i,n}) = S_{c,i,n}/(S_{c,i,n} + I_{c,i,n} + \sigma_{\text{BS}}^2)$, the remaining fractional term has an affine denominator in the optimization variables.

b) Quadratic transform for fractional SINR terms: We next apply the quadratic transform [45] by introducing auxiliary variables $\rho_{c,i,n} \in \mathbb{R}$ for $i \in \{1, 2\}$ and $n \in \mathcal{N}$. Define the constant and numerator terms as

$$\begin{aligned} A_{i,n} &\triangleq \log_2(1 + \alpha_{c,i,n}) - \alpha_{c,i,n} \log_2 e, \\ B_{i,n} &\triangleq \sqrt{(1 + \alpha_{c,i,n}) S_{c,i,n}}, \\ C_{i,n} &\triangleq S_{c,i,n} + I_{c,i,n} + \sigma_{\text{BS}}^2. \end{aligned} \quad (52)$$

The quadratic-transform surrogate rate on subcarrier n is then

$$\tilde{R}_{c,i,n} = A_{i,n} + (2\rho_{c,i,n} B_{i,n} - \rho_{c,i,n}^2 C_{i,n}) \log_2 e, \quad (53)$$

for $i \in \{1, 2\}$. For the supplementary stream ($i = 2$), the interference term consists of the linearized mismatch surrogate

in (50) together with the uncancelable echo-path ICI from the supplementary stream itself

$$I_{c,2,n} \triangleq \tilde{P}_{\text{mismatch},n}(\mathbf{p}, \mathbf{X}) + \sum_{k \neq n} \xi_{n,k} |H_{\text{EP},k}[m]|^2 p_{c,2}[k]. \quad (54)$$

For fixed $(\mathbf{p}, \mathbf{X}, \boldsymbol{\alpha})$, the optimal quadratic-transform auxiliary variables are updated in closed form as [45]:

$$\rho_{c,i,n}^* = \frac{B_{i,n}}{C_{i,n}}, \quad i \in \{1, 2\}. \quad (55)$$

c) *Quadratic transform for sensing epigraph constraints:*

For the sensing constraint, we introduce real auxiliary variables $y_n \geq 0$ and rewrite $z_n \leq \gamma_{r,n}(\mathbf{p})$ equivalently as [45]:

$$z_n \leq 2y_n \sqrt{S_{r,n}(\mathbf{p})} - y_n^2 (I_{r,n}(\mathbf{p}) + \sigma_{\text{BS}}^2), \quad \forall n \in \mathcal{N}. \quad (56)$$

For fixed \mathbf{p} , the optimal update is computed as [45]

$$y_n^* = \frac{\sqrt{S_{r,n}(\mathbf{p})}}{I_{r,n}(\mathbf{p}) + \sigma_{\text{BS}}^2}.$$

d) *Max-SE design with a sensing target:* For fixed auxiliary variables $\{\boldsymbol{\alpha}, \boldsymbol{\rho}, \mathbf{y}\}$ and fixed Taylor reference points $\{\mathbf{p}^{(i)}, \mathbf{X}^{(i)}\}$, the convex conic subproblem is

$$\max_{\mathbf{p}, \mathbf{X}, \mathbf{z}} \sum_{n \in \mathcal{N}} \left(\tilde{R}_{c,1,n}(\mathbf{p}) + \tilde{R}_{c,2,n}(\mathbf{p}, \mathbf{X}) \right) \quad (57a)$$

$$\text{s.t. } \text{Tr}(\mathbf{W}\mathbf{X}) \leq \Gamma_{\text{sens}}, \quad (57b)$$

$$\mathbf{z} \succeq \mathbf{0}, \quad (57c)$$

$$\mathbf{J}(\mathbf{z}) \triangleq \sum_{n \in \mathcal{N}} z_n \mathbf{K}_n \succeq \delta \mathbf{I}_2, \quad (57d)$$

$$\begin{bmatrix} \mathbf{X} & \mathbf{I}_2 \\ \mathbf{I}_2 & \mathbf{J}(\mathbf{z}) \end{bmatrix} \succeq \mathbf{0}, \quad (57e)$$

$$z_n \leq 2y_n \sqrt{S_{r,n}(\mathbf{p})} - y_n^2 (I_{r,n}(\mathbf{p}) + \sigma_{\text{BS}}^2), \quad \forall n, \quad (57f)$$

$$(43c), (43d), (43e). \quad (57g)$$

In (57f), y_n is the auxiliary variable associated with the quadratic transform of the sensing SINR constraint. Problem (57) is a convex semidefinite program (SDP) that can be solved efficiently using interior-point methods.

V. NUMERICAL RESULTS

In this section, we evaluate the proposed RS-inspired bistatic OFDM-ISAC framework through Monte Carlo simulations. The system and algorithmic parameters are summarized in Table I. We adopt a subcarrier spacing of $\Delta f = 15$ kHz and consider an OFDM grid with $N_{\text{sc}} = 32$ active subcarriers. For a given Doppler shift, larger subcarrier spacings reduce the normalized Doppler $\nu_{\text{tar}}/\Delta f$ and therefore mitigate ICI [46]; the present choice is made so that the impact of uncompensated EP ICI remains visible under vehicular mobility, while the joint optimization remains computationally tractable.

The proposed framework is benchmarked against two NOMA-inspired baselines, each obtained as a special case of the RS-inspired architecture by deactivating one of the communication streams. The first, **NOMA-CF** (*Communication-First*), sets $p_{c,2}[n] = 0$, so that all communication power is allocated to the robust stream $s_{c,1}$, while the EP contribution is treated

Table I: Simulation Parameters and Experimental Scenarios

Parameter	Value
System and Waveform Configuration	
Carrier Frequency (f_c)	28 GHz [47]
Subcarrier Spacing (Δf)	15 kHz
Number of Active Subcarriers (N_{sc})	32 [17]
Max. Transmit Power (P_{tx})	23 dBm
Effective Noise Floor (σ_{BS}^2)	-95 dBm
Network Geometry & Channel Models	
Base Station (BS) Position	(0, 0) m
Vehicular UE Position	(300, 0) m
Sensing Target Position	(250, 50) m
DP Channel Model	3GPP TDL-C [47]
DP Delay Spread	1000 ns
Effective Sensing-Link Antenna Gain	38 dBi
Target RCS ($\sigma_{\text{RCS}}^{\text{bi}}$)	10 m ² (10 dBsm)
Optimization Constraints	
Integration Pulses (M)	16
Max. BCD Iterations	25
Convergence Tolerance	10 ⁻⁴
Power Allocation Mask ($P_{\text{min}}, P_{\text{max}}$)	$P_{\text{avg}} \pm 5\%$
Evaluated Scenarios	
$\Delta G_{\text{DP-EP}}$ sweep	~ 13.6 to 28.6 dB
Static ($v = 0$ km/h)	$\Gamma_{\text{sens}} \in \{100, 200\}$
Moderate mobility	$v_{\text{UE}} = 40, v_{\text{t}} = 60$ km/h
Severe mobility	$v_{\text{UE}} = 80, v_{\text{t}} = 120$ km/h
Monte Carlo runs	1000 per realization

as uncancelled interference during communication decoding. The second, **NOMA-SF** (*Sensing-First*), sets $p_{c,1}[n] = 0$, so that all communication power is allocated to the supplementary stream $s_{c,2}$ and decoding relies on prior echo estimation and cancellation. An OMA-inspired baseline is not included, since prior studies have already shown orthogonal resource-separation to be less effective than non-orthogonal designs for interference management in ISAC, while also incurring a SE penalty [2], [3], [17]. Next, to assess the framework across different interference regimes, performance is evaluated as a function of the relative interference gain DP/EP gap $\Delta G_{\text{DP-EP}}$. For sensing, we adopt $\Gamma_{\text{sens}} \in \{100, 200\}$ as the maximum tolerable weighted A-optimal CRLB target, which jointly constrains delay and Doppler estimation errors after physical normalization [43]. The numerical study is organized into two parts:

- **Part I: IFI Analysis.** With kinematic parameters set to zero, we isolate the coupling between sensing accuracy and communication throughput. We evaluate the framework's ability to manage IFI under a weighted A-optimal CRLB target, Γ_{sens} , which jointly constrains range and velocity estimation errors in m² and (m/s)², respectively. This includes a subcarrier-level analysis of radar power allocation and a SE comparison of the proposed RS-inspired scheme against the NOMA baselines.
- **Part II: Joint IFI and ICI Management.** Building upon the baseline established in Part I, we introduce the kinematic parameters to evaluate the framework under the coupled impairments of IFI and Doppler-induced ICI. This part focuses on how uncompensated echo ICI induces severe reconstruction mismatches and self-interference, fundamentally altering the relative performance gains across different mobility profiles and throughout the entire relative interference spectrum.

Before turning to these two parts, we first examine the convergence behavior of the proposed optimization framework under both static and high-mobility conditions.

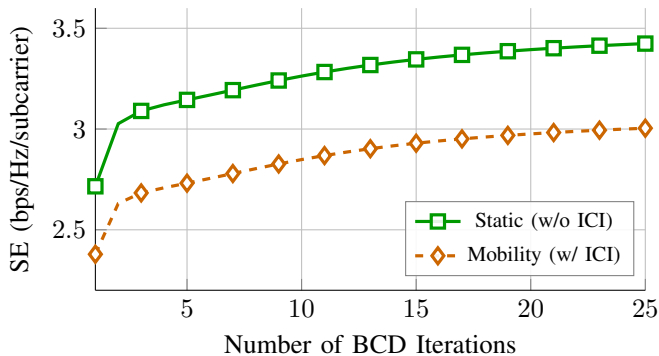


Figure 3: Convergence profile of the proposed RS-inspired BCD algorithm in terms of average SE per subcarrier.

Figure 3 shows the average convergence trajectory of the proposed RS-inspired algorithm over 25 iterations. In both the static and high-mobility cases, the objective exhibits monotonic non-decreasing behaviour, consistent with the underlying fractional-programming-based AO procedure. The algorithm converges rapidly, attaining most of its steady-state SE within approximately 5–10 iterations, which is important for vehicular ISAC settings with limited channel coherence time. The high-mobility curve follows a similar convergence pattern to the static case, but with a downward shift caused by the SINR degradation induced by Doppler-leakage ICI.

A. IFI Analysis

To isolate the fundamental sensing–communication coupling from the additional effects of Doppler-induced ICI, we first consider the zero-mobility regime. Figure 4 shows the power allocation for a representative channel realization, comparing the proposed RS-inspired framework with the two baselines. The corresponding allocations are overlaid with the normalized DP channel magnitude $|H_{DP}|^2$ in order to illustrate how the optimizer adapts to the underlying fading profile.

As expected, all architectures allocate a significant fraction of the radar-sequence power p_r to the edge subcarriers, where the FIM is most sensitive to frequency diversity and the sensing target $\Gamma_{\text{sens}} \leq 200$ can be met more efficiently. However, the two NOMA-inspired baselines exhibit a near-orthogonal allocation pattern, with communication and radar resources becoming effectively separated over large portions of the band. This behavior reflects the rigidity of their decoding structures: once the optimizer encounters strong IFI bottlenecks, it reduces overlap between communication and sensing rather than sustaining a fully non-orthogonal solution. As a result, NOMA-CF and NOMA-SF achieve SEs of only 2.12 bps/Hz and 2.24 bps/Hz, respectively.

By contrast, the proposed RS-inspired framework exploits a substantially richer feasible region and achieves a higher sum-rate of 2.67 bps/Hz. Notably, this improvement is obtained even though the RS-inspired design allocates a larger fraction of the total power to the radar sequence than the NOMA-inspired

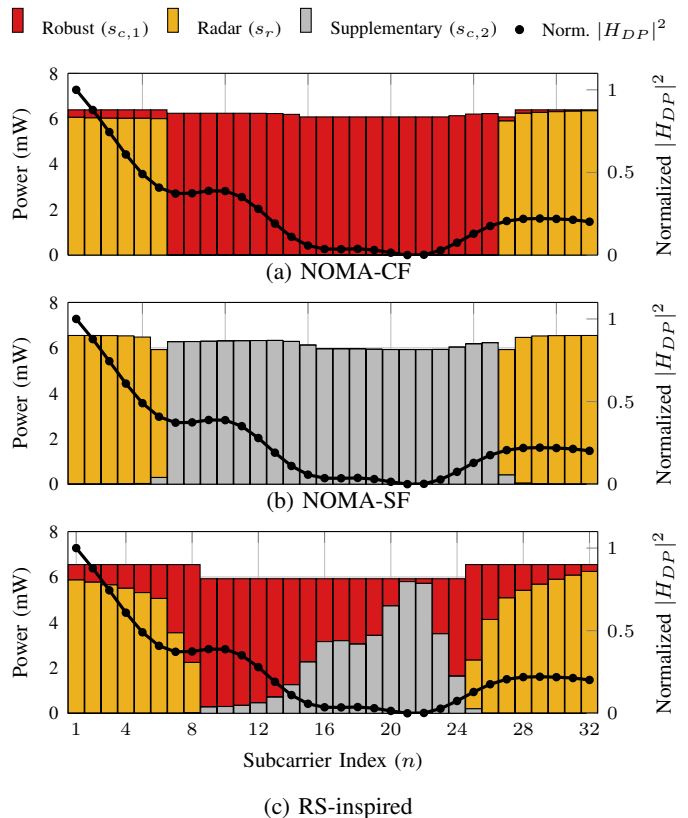


Figure 4: Power allocation across different architectures.

baselines. The gain stems from the flexible superposition structure: most communication power is assigned to the robust stream $s_{c,1}$, while the supplementary stream $s_{c,2}$ is more selectively deployed. Since the DP radar contribution is cancelled prior to sensing, the robust stream can coexist more freely with the radar sequence, leaving only its weak EP contribution to affect sensing. In contrast, the supplementary stream is constrained more tightly, since it not only affects the sensing SINR in Step 3 but is also limited by the reconstruction mismatch and residual self-interference appearing in Step 4. Accordingly, the optimizer allocates $s_{c,2}$ power to subcarriers where its impact on sensing is less detrimental, which in turn improves the reliability of its own subsequent decoding, while allowing $s_{c,1}$ to carry the bulk of the communication load.

To evaluate performance over a broader range of interference conditions, we next sweep ΔG_{DP-EP} , thereby transitioning from a strong-echo regime (small ΔG_{DP-EP}) to a DP-dominated regime (large ΔG_{DP-EP}). This sweep captures the spatial power imbalance that is intrinsic to bistatic ISAC deployments. Figure 5 reports the average SE of all architectures as a function of ΔG_{DP-EP} under zero-mobility conditions.

For small ΔG_{DP-EP} , the echo remains sufficiently strong to enable accurate target-parameter estimation, so sensing-first cancellation becomes effective. Consequently, both NOMA-SF and the proposed RS-inspired framework significantly outperform NOMA-CF with a gain of $\simeq 30\%$, which treats the comparatively strong echo as residual interference and therefore suffers a substantial SINR penalty. As ΔG_{DP-EP} increases and the direct path becomes dominant, this trend reverses: NOMA-CF improves steadily, whereas NOMA-SF

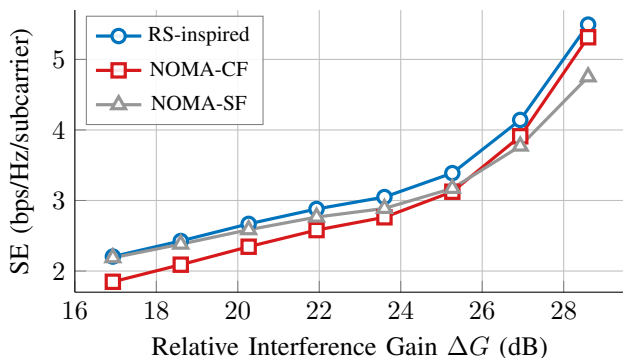


Figure 5: Average SE vs. ΔG_{DP-EP} , comparing the RS-inspired against NOMA-CF and NOMA-SF.

deteriorates because echo estimation becomes less reliable and reconstruction errors translate into residual interference after cancellation. The RS-inspired framework, however, maintains a strictly positive performance gap throughout the entire sweep. Near $\Delta G_{DP-EP} \approx 25$ dB, the two NOMA-inspired baselines achieve nearly identical SE, indicating that, regardless of the decoding order, the system remains fundamentally interference-limited by the coupling between sensing and communication. In this same region, the proposed RS-inspired framework achieves its largest gain over the stronger of the two NOMA-inspired baselines, underscoring that RS-inspired processing provides a more general and robust interference-management principle than either fixed sensing-first or fixed communication-first decoding. Finally, at very high ΔG_{DP-EP} , RS-inspired and NOMA-CF significantly outperform NOMA-SF, by $\approx 17\%$.

To further quantify this behaviour under more stringent sensing requirements, we examine three representative operating conditions of the ΔG_{DP-EP} sweep through two compact views: an edge-regime comparison, capturing the relatively strong-echo and DP-dominated cases, and an intermediate-regime comparison near the NOMA-baseline intersection. In each case, the performance is evaluated for $\Gamma_{sens} \in \{100, 200\}$.

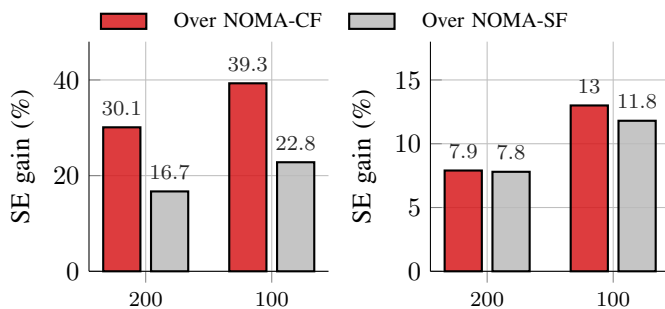


Figure 6: SE gain of RS-inspired framework over baselines for $\Gamma_{sens} \in \{200, 100\}$: (a) edge regimes, with gain over NOMA-CF at $\Delta G_{DP-EP} = 14$ dB and over NOMA-SF at $\Delta G_{DP-EP} = 29$ dB; (b) intermediate regime at $\Delta G_{DP-EP} = 25$ dB.

Tightening the sensing constraint forces the optimizer to allocate more resources to the radar sequence, thereby increasing the pressure on the communication streams. This effect is examined through two complementary views. In the edge-regime comparison, the gain of RS-inspired framework over NOMA-

CF in the strong-echo regime and over NOMA-SF in the DP-dominated regime both increase as Γ_{sens} is tightened from 200 to 100. This confirms that stricter sensing requirements amplify the structural limitations of the fixed-order NOMA-inspired baselines at the two ends of the interference spectrum. In the intermediate regime near $\Delta G_{DP-EP} \approx 25$ dB, where the two NOMA-inspired baselines achieve nearly identical SE, the advantage of the proposed framework also increases under the tighter sensing target, with gains rising from about 7.8% at $\Gamma_{sens} = 200$ to above 11% at $\Gamma_{sens} = 100$. At $\Gamma_{sens} = 100$, the gain over NOMA-CF reaches 13.0%, while the gain over NOMA-SF is 11.8%. This asymmetry is also informative: under more stringent sensing requirements, the larger radar allocation causes stronger uncanceled echo interference for NOMA-CF, whereas NOMA-SF remains partially protected by echo estimation and cancellation prior to communication decoding. Overall, these results show that the proposed RS-inspired architecture remains consistently advantageous across both edge and intermediate regimes, and that its benefit becomes more pronounced as the sensing requirement tightens.

B. Joint IFI and ICI Management

We now extend the analysis to the mobility regime, where Doppler-induced ICI appears on the echo path. While DP ICI is assumed compensated at the receiver, the uncompensated EP ICI destroys subcarrier orthogonality in the sensing return and thereby compounds the IFI already observed in the static case. To isolate this effect, Fig. 7 reports the relative SE gain of RS-inspired framework over the NOMA-inspired baselines across different velocity profiles, considering both the edge regimes of the ΔG_{DP-EP} sweep and the intermediate regime near the NOMA-baseline intersection. Figure 7 reveals that the impact of mobility depends strongly on the operating regime. In the strong-echo regime, RS-inspired framework benefits from the availability of a strong echo path and therefore outperform NOMA-CF, which treats the echo as residual interference. As mobility increases, however, Doppler-induced ICI progressively reduces the usefulness of the echo for sensing-first processing, so the relative advantage over NOMA-CF decreases. In the DP-dominated regime, the gain of RS-inspired framework over NOMA-SF is non-monotonic with mobility. At moderate mobility, the gain decreases slightly because the RS-inspired design already places most of its communication power on the robust stream, whose decoding is increasingly penalized by echo-path ICI, while NOMA-SF can still exploit the echo reasonably effectively.

At high mobility, however, the weak echo becomes sufficiently Doppler-corrupted that sensing-first cancellation deteriorates rapidly. As a result, NOMA-SF degrades more severely, whereas the RS-inspired framework remains more robust by relying primarily on the DP-supported robust stream, thereby recovering and increasing its relative advantage. The intermediate regime near the NOMA-baseline intersection (bottom panel) exhibits a non-monotonic response with respect to both baselines. Over NOMA-CF, the gain of RS-inspired framework first increases at moderate mobility, because echo-path ICI directly elevates the interference floor of the communication-first

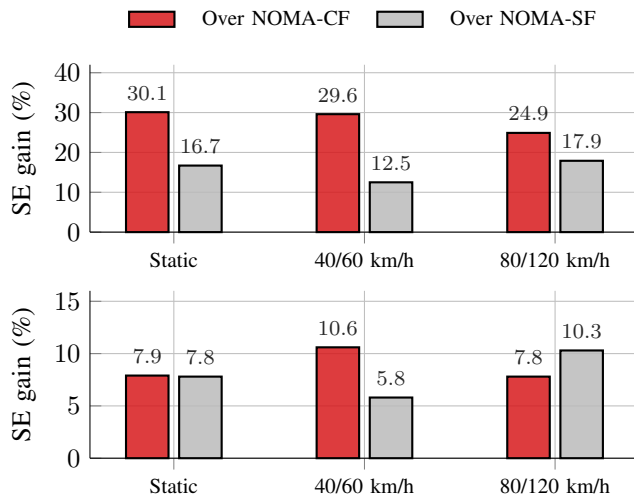


Figure 7: SE gain of RS-inspired over baselines across mobility scenarios. Top: edge-regime, showing the gain over NOMA-CF at $\Delta G_{DP-EP} = 14$ dB and over NOMA-SF at $\Delta G_{DP-EP} = 29$ dB. Bottom: intermediate regime at $\Delta G_{DP-EP} = 25$ dB.

baseline, and then decreases at high mobility as reconstruction mismatch and self-ICI also begin to penalize the proposed design. Over NOMA-SF, the trend is similar to that observed in the DP-dominated edge regime: the gain first decreases at moderate mobility and then rises sharply at high mobility, for the same reason that sensing-first cancellation remains effective only while Doppler-induced corruption of the echo remains limited. To determine whether these trends persist beyond the

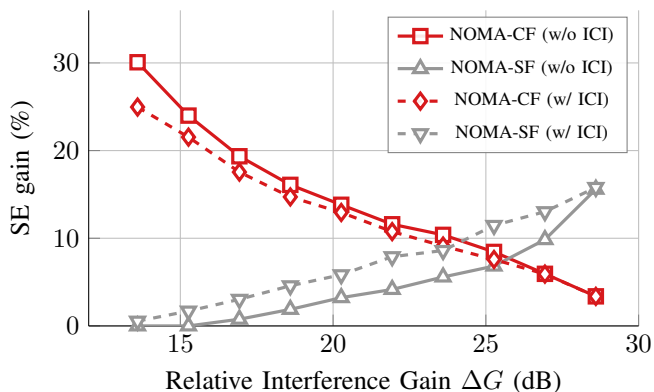


Figure 8: SE gain of the RS-inspired over NOMA-inspired vs. ΔG_{DP-EP} : static vs. high-mobility (ICI).

representative regimes shown in Fig. 7, we next evaluate the full ΔG_{DP-EP} sweep under high mobility. Fig. 8 shows the RS relative gain over each NOMA baseline across the ΔG_{DP-EP} sweep. As expected, the gain over NOMA-CF decreases with ΔG_{DP-EP} , while the gain over NOMA-SF follows the opposite trend. Under high mobility, the gain over NOMA-SF is strictly positive and substantially larger than in the static case: severe Doppler spread corrupts radar parameter estimation, causing SIC reconstruction mismatches and unmitigated self-interference in NOMA-SF, whereas the RS framework mitigates this collapse by dynamically reducing power on the vulnerable supplementary stream. Conversely, the presence of ICI reduces

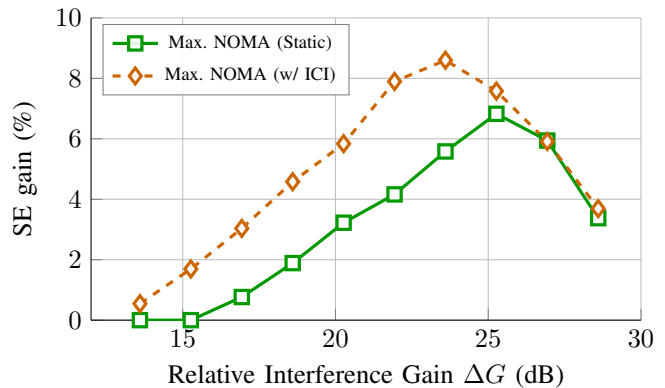


Figure 9: SE gain of RS-inspired over baselines envelope.

the relative gain over NOMA-CF in the low- ΔG_{DP-EP} regime, where the echo remains sufficiently strong to be exploitable. As ΔG_{DP-EP} increases, the relative-gain curves with respect to the two baselines converge, since the compensated direct path progressively dominates the communication link and the effect of echo-path ICI becomes less pronounced. The crossover point also shifts leftward under mobility, indicating that once the echo becomes sufficiently Doppler-corrupted, treating it as interference becomes preferable to attempting cancellation at an earlier point in the sweep.

To consolidate the comparison, Fig. 9 benchmarks the proposed framework against the NOMA envelope, defined as the pointwise maximum of the two baselines, i.e., $\max(SE_{NOMA-CF}, SE_{NOMA-SF})$. By doing so, we explicitly analyse the fundamental gains achieved through RS's IFI management from the artifacts of ICI mitigation. The static curve in Fig. 9 captures the gain attributable to more flexible IFI management alone. Under high mobility, the gain increases over the low-to-medium ΔG_{DP-EP} regime, showing that the proposed framework offers an additional robustness advantage against echo-path ICI. The vertical separation between the static and high-mobility curves therefore quantifies the portion of the gain associated with ICI resilience, beyond the baseline inter-functionality gain already present in the static setting. Consistent with Fig. 8, uncompensated echo-path ICI shifts the peak gain leftward, indicating that the NOMA envelope transitions earlier toward interference-limited operation in which sensing-first cancellation is no longer beneficial. Finally, at sufficiently large ΔG_{DP-EP} , the two curves converge, as the direct path dominates, the influence of echo-path ICI diminishes, and the RS-inspired solution approaches to NOMA-CF.

VI. CONCLUSION

This paper investigated an RS-inspired uplink bistatic OFDM-ISAC framework for jointly managing IFI and echo-path ICI. The proposed design combines a staged receiver with a sensing-constrained power-allocation strategy, thereby linking sensing accuracy and communication reliability through the echo-channel reconstruction error. Based on this framework, tractable per-subcarrier SINR expressions, a weighted A-optimal CRLB characterization, and a tractable optimization method based on LMI reformulation, convex surrogates, and multidimensional fractional programming were developed. Numerical results

showed that the proposed RS-inspired design generalises and consistently outperforms NOMA-inspired baselines. In the zero-mobility regime, the gain arises from more flexible IFI management, while under mobility the proposed framework also exhibits stronger robustness to echo-path ICI. These results highlight the potential of RS-inspired staged processing for uplink bistatic vehicular ISAC in doubly selective channels. Future work may extend to multi-target and multi-antenna settings, imperfect DP cancellation, and adaptive waveform or numerology design for mobility-aware bistatic ISAC.

REFERENCES

- [1] F. Liu *et al.*, "Integrated Sensing and Communications: Toward Dual-Functional Wireless Networks for 6G and Beyond," *IEEE J. Sel. Areas Commun.*, vol. 40, no. 6, pp. 1728–1767, 2022.
- [2] X. Mu *et al.*, "NOMA for Integrating Sensing and Communications Toward 6G: A Multiple Access Perspective," *IEEE Wireless Commun.*, vol. 31, no. 3, pp. 316–323, 2024.
- [3] A. Mishra *et al.*, "Coexistence of Radar and Communication with Rate-Splitting Wireless Access," *IEEE Commun. Lett.*, pp. 1–1, 2025.
- [4] F. Liu *et al.*, "Joint Radar and Communication Design: Applications, State-of-the-Art, and the Road Ahead," *IEEE Trans. Commun.*, vol. 68, no. 6, pp. 3834–3862, 2020.
- [5] A. Mishra *et al.*, "Temporal Windows of Integration for Multisensory Wireless Systems as Enablers of Physical AI," *arXiv preprint arXiv:2512.09589*, 2025.
- [6] K. Chen *et al.*, "Interference Management for Integrated Sensing and Communications: A Multiple Access Perspective," *arXiv preprint arXiv:2509.02352*, 2025.
- [7] C. Ouyang *et al.*, "On the Performance of Uplink ISAC Systems," *IEEE Commun. Lett.*, vol. 26, no. 8, pp. 1769–1773, 2022.
- [8] A. R. Chiriyath *et al.*, "Inner Bounds on Performance of Radar and Communications Co-Existence," *IEEE Trans. Signal Process.*, vol. 64, no. 2, pp. 464–474, 2016.
- [9] Z. Wei *et al.*, "Integrated Sensing and Communication Signals Toward 5G-A and 6G: A Survey," *IEEE Internet Things J.*, vol. 10, no. 13, pp. 11 068–11 092, 2023.
- [10] C. Zhang *et al.*, "Semi-Integrated-Sensing-and-Communication (Semi-ISAC): From OMA to NOMA," *IEEE Trans. Commun.*, vol. 71, no. 4, pp. 1878–1893, 2023.
- [11] D. Brunner *et al.*, "Bistatic OFDM-Based ISAC With Over-the-Air Synchronization: System Concept and Performance Analysis," *IEEE Trans. Microw. Theory Techn.*, vol. 73, no. 5, pp. 3016–3029, 2025.
- [12] P. Schniter, "Low-complexity equalization of OFDM in doubly selective channels," *IEEE Trans. Signal Process.*, vol. 52, no. 4, pp. 1002–1011, 2004.
- [13] Z. Yu *et al.*, "A framework for uplink ISAC receiver designs: performance analysis and algorithm development," *arXiv:2503.02647*, 2025.
- [14] F. Zhang *et al.*, "Joint Range and Velocity Estimation With Intrapulse and Intersubcarrier Doppler Effects for OFDM-Based RadCom Systems," *IEEE Trans. Signal Process.*, vol. 68, pp. 662–675, 2020.
- [15] M. M. Sahin *et al.*, "Multicarrier Rate-Splitting Multiple Access: Superiority of OFDM-RSMA Over OFDMA and OFDM-NOMA," *IEEE Commun. Lett.*, vol. 27, no. 11, 2023.
- [16] A. Mishra *et al.*, "Rate-Splitting Multiple Access for 6G—Part I: Principles, Applications and Future Works," *IEEE Commun. Lett.*, vol. 26, no. 10, pp. 2232–2236, 2022.
- [17] M. M. Sahin *et al.*, "OFDM-RSMA: Robust Transmission Under Inter-Carrier Interference," *IEEE Trans. Commun.*, vol. 73, no. 7, 2025.
- [18] A. Mishra *et al.*, "Rate-Splitting Multiple Access for Downlink Multiuser MIMO: Precoder Optimization and PHY-Layer Design," *IEEE Trans. Commun.*, vol. 70, no. 2, pp. 874–890, 2022.
- [19] Y. Li *et al.*, "Performance Analysis of Uplink Joint Communication and Sensing System," in *Proc. IEEE/CIC Int. Conf. Commun. China (ICCC)*, 2022, pp. 588–593.
- [20] C. Xu *et al.*, "Rate-Splitting Multiple Access for Multi-Antenna Joint Radar and Communications," *IEEE J. Sel. Topics Signal Process.*, vol. 15, no. 6, pp. 1332–1347, 2021.
- [21] L. Yin *et al.*, "Rate-Splitting Multiple Access for 6G—Part II: Interplay With Integrated Sensing and Communications," *IEEE Commun. Lett.*, vol. 26, no. 10, pp. 2237–2241, 2022.
- [22] C. Hu *et al.*, "Joint Transmit and Receive Beamforming Design for Uplink RSMA Enabled Integrated Sensing and Communication Systems," in *Proc. IEEE Wireless Commun. Netw. Conf. (WCNC)*, 2023, pp. 1–6.
- [23] Z. Wang *et al.*, "NOMA Inspired Interference Cancellation for Integrated Sensing and Communication," in *Proc. IEEE Int. Conf. Commun. (ICC)*, 2022, pp. 3154–3159.
- [24] V. Tapio *et al.*, "Bi-Static Sensing with 5G NR Physical Uplink Shared Channel Transmission," in *Proc. IEEE 4th Int. Symp. Joint Commun. Sens. (JC&S)*, 2024, pp. 1–6.
- [25] J. Park *et al.*, "RSMA-Based Bistatic ISAC Framework for LEO Satellite Systems," in *Proc. IEEE Int. Conf. Commun. Workshops (ICC Workshops)*, 2024, pp. 1840–1845.
- [26] N. J. Willis, *Bistatic Radar*, Chapter 25, 2nd ed. The Institution of Engineering and Technology, 2004.
- [27] C. Sturm and W. Wiesbeck, "Waveform Design and Signal Processing Aspects for Fusion of Wireless Communications and Radar Sensing," *Proc. IEEE*, vol. 99, no. 7, pp. 1236–1259, 2011.
- [28] A. Mishra *et al.*, "Rate-Splitting assisted massive Machine-Type Communications in Cell-Free Massive MIMO," *IEEE Commun. Lett.*, pp. 1–1, 2022.
- [29] A. Mishra, "Advancing multi-antenna technologies for 6G: rate-splitting multiple access, (cell-free) Massive MIMO, reconfigurable intelligent surfaces," Oct 2023. [Online]. Available: <http://hdl.handle.net/10044/1/111358>
- [30] A. Mishra *et al.*, "Mitigating intra-cell pilot contamination in massive MIMO: A rate splitting approach," *IEEE Trans. Wirel. Commun.*, vol. 22, no. 5, pp. 3472–3487, 2022.
- [31] J. Park *et al.*, "A Bistatic ISAC Framework for LEO Satellite Systems: A Rate-Splitting Approach," *IEEE Trans. Aerosp. Electron. Syst.*, pp. 1–19, 2025.
- [32] B. Wang *et al.*, "Cramer-Rao Lower Bound Analysis for OTFS and OFDM Modulation Systems," in *Proc. Int. Symp. Wireless Pers. Multimedia Commun. (WPMC)*, 2023, pp. 1–6.
- [33] T. Chen *et al.*, "Location-Based Timing Advance Estimation for 5G Integrated LEO Satellite Communications," in *Proc. IEEE Global Commun. Conf. (GLOBECOM)*, 2020, pp. 1–6.
- [34] J. L. Garry *et al.*, "Evaluation of Direct Signal Suppression for Passive Radar," *IEEE Trans. Geosci. Remote Sens.*, vol. 55, no. 7, pp. 3786–3799, 2017.
- [35] A. Masmoudi and T. Le-Ngoc, "Channel estimation and self-interference cancellation in full-duplex communication systems," *IEEE Trans. Veh. Technol.*, vol. 66, no. 1, pp. 321–334, 2017.
- [36] P. Moose, "A technique for orthogonal frequency division multiplexing frequency offset correction," *IEEE Trans. Commun.*, vol. 42, no. 10, pp. 2908–2914, 1994.
- [37] S. M. Kay, *Fundamentals of Statistical Signal Processing: Estimation Theory*. Upper Saddle River, NJ: Prentice-Hall, 1993.
- [38] D. Tse and P. Viswanath, *Fundamentals of Wireless Communication*. Cambridge: Cambridge University Press, 2005.
- [39] Z. Bai *et al.*, "Dual-Scale Channel Estimation in Sensing-Assisted Communication Systems: Joint Time Allocation and Beamforming Design," Jan. 2026, arXiv:2411.05267v2, 1 Jan 2026.
- [40] H. Benaroya *et al.*, *Probability Models in Engineering and Science*, ser. Advanced topics in mechanical engineering series. Taylor & Francis, 2005.
- [41] Y. Liu *et al.*, "Multiobjective optimal waveform design for OFDM integrated radar and communication systems," *Signal Process.*, vol. 141, pp. 331–342, 2017.
- [42] M. Braun *et al.*, "Maximum likelihood speed and distance estimation for OFDM radar," in *2010 IEEE Radar Conference*, 2010, pp. 256–261.
- [43] M. Zhu *et al.*, "Information and sensing beamforming optimization for multi-user multi-target MIMO ISAC systems," *EURASIP J. Adv. Signal Process.*, vol. 2023, no. 1, p. 15, 2023.
- [44] S. Joshi and S. Boyd, "Sensor Selection via Convex Optimization," *IEEE Trans. Signal Process.*, vol. 57, no. 2, pp. 451–462, 2009.
- [45] K. Shen and W. Yu, "Fractional Programming for Communication Systems—Part I: Power Control and Beamforming," *IEEE Trans. Signal Process.*, vol. 66, no. 10, pp. 2616–2630, 2018.
- [46] T. V. S. Sreedhar and N. B. Mehta, "Refined bounds for inter-carrier interference in ofdm due to time-varying channels and phase noise," *IEEE wireless communications letters*, vol. 11, no. 12, pp. 2522–2526, 2022.
- [47] 3GPP, "Study on channel model for frequencies from 0.5 to 100 GHz," 3rd Generation Partnership Project (3GPP), Technical Report (TR) 38.901 V19.1.0, Sep. 2025, release 19.